MICROROBOTS

Magnetically actuated gearbox for the wireless control of millimeter-scale robots

Chong Hong[1,2]†, Ziyu Ren[1,3]†, Che Wang[2], Mingtong Li[1], Yingdan Wu[1], Dewei Tang[2], Wenqi Hu[1]*, Metin Sitti[1,3,4]*

The limited force or torque outputs of miniature magnetic actuators constrain the locomotion performances and functionalities of magnetic millimeter-scale robots. Here, we present a magnetically actuated gearbox with a maximum size of 3 millimeters for driving wireless millirobots. The gearbox is assembled using microgears that have reference diameters down to 270 micrometers and are made of aluminum-filled epoxy resins through casting. With a magnetic disk attached to the input shaft, the gearbox can be driven by a rotating external magnetic field, which is not more than 6.8 millitesla, to produce torque of up to 0.182 millinewton meters at 40 hertz. The corresponding torque and power densities are 12.15 micronewton meters per cubic millimeter and 8.93 microwatt per cubic millimeter, respectively. The transmission efficiency of the gearbox in the air is between 25.1 and 29.2% at actuation frequencies ranging from 1 to 40 hertz, and it lowers when the gearbox is actuated in viscous liquids. This miniature gearbox can be accessed wirelessly and integrated with various functional modules to repeatedly generate large actuation forces, strains, and speeds; store energy in elastic components; and lock up mechanical linkages. These characteristics enable us to achieve a peristaltic robot that can crawl on a flat substrate or inside a tube, a jumping robot with a tunable jumping height, a clamping robot that can sample solid objects by grasping, a needle-puncture robot that can take samples from the inside of the target, and a syringe robot that can collect or release liquids.

INTRODUCTION

Magnetic actuation allows fast, precise, wireless, and dexterous force and torque generation for magnetic millirobots in confined workspaces (*1*–*5*). In many applications at the millimeter scale, actuation forces as high as several hundreds of millinewtons are required to penetrate biological tissues (*6*), open a collapsed space (*7*), or apply a force normal to the substrate for adhesion (*8*). However, as the robot size, L, decreases, the magnetic force and torque scale down rapidly with L^2–L^4 (*9*, *10*), which limits the performance of these robots.

Given the size of a magnetic actuator, the magnetic force and torque outputs are proportional to the gradient and strength of the external magnetic field and the magnetization of the magnetic materials. Capped by the maximum remnant magnetization of the available magnetic materials (*11*), previous studies have proposed various strategies to enhance the external magnetic field to augment the force and torque outputs of the magnetic actuators. As the most straightforward way, a powerful permanent magnet can be used to produce a torque of around 0.4 nNm to actuate a single flexible tapered foot at magnetic fields up to 200 mT, driving the motion of a multilegged soft millirobot (*12*). However, this method requires placing the magnet very close to the robot to achieve a substantially high magnetic field strength, limiting its application in scenarios where the robots function far away from the source of the magnetic field, such as controlling microrobots deep inside the human body (*13*). In addition, permanent magnets can also be arranged into different patterns to obtain a high magnetic field gradient (on the order of 7 T/m) for a magnetic pulling force at dozens of millinewtons (*14*). However, the workspace obtained through this method is limited to the centimeter scale, and simply scaling up the design will decrease the strength of the magnetic field.

For electromagnetic actuation systems, pushing the electrical current limit of the electromagnets can augment the maximum possible magnetic field strengths, which could be much larger than the ones that permanent magnets can produce. In (*15*), electrical currents of up to 140 A were applied to each coil stack to produce a magnetic field strength of up to 400 mT and a magnetic field gradient of up to 3 T/m. Such a strong magnetic field can drive a permanent magnet to drill through gels or a raw pork fillet. However, these high-power electromagnets require a cooling system with a high cooling capacity, which makes the system bulky and expensive. Although even stronger magnetic fields can be produced by magnetic resonance imaging scanners (*16*, *17*) and high-temperature superconducting magnets (*18*), these strong magnetic fields will remagnetize the magnetic materials with preprogrammed magnetizations. Many magnetic robots have required maximum magnetic field strengths. For example, magnetic microrollers coated with a nickel layer can only properly function under magnetic fields below 20 mT; otherwise, they cannot retain their magnetization direction (*19*).

In addition to pushing the limits of the external magnetic field strength, amplifying the magnetic torque and force outputs through a mechanical transmission system is a promising alternative. The gear train is one of the most widely used transmission systems to amplify the exerted torque or force and has been achieved in many microsystems for various on-chip applications (*20*–*23*). The gearboxes have also been applied in large-scale magnetically driven devices (*24*, *25*). These designs are similar to the transmission of many cable-driven robots in which the speed reducers are separated from the motor and located at the joint of the arms (*26*–*28*). In this

[1]Physical Intelligence Department, Max Planck Institute for Intelligent Systems, 70569 Stuttgart, Germany. [2]State Key Laboratory of Robotics and Systems, Harbin Institute of Technology, Harbin 150080, China. [3]Institute for Biomedical Engineering, ETH Zürich, 8092 Zürich, Switzerland. [4]School of Medicine and College of Engineering, Koç University, 34450 Istanbul, Turkey.
*Corresponding author. Email: wenqi@is.mpg.de (W.H.); sitti@is.mpg.de (M.S.)
†These authors contributed equally to this work.

way, the magnetic torque or force is amplified, and the transmission stiffness is increased. All of these merits motivated us to develop miniature gearboxes for magnetically driven mobile millirobots to achieve better locomotion capabilities and different robotic functions. Although miniature gearboxes have been used in millirobots driven by electrical motors (*29*, *30*), difficulties in integrating onboard power sources prevent these robots from being wireless. We foresee that by combining magnetic actuation and miniature gearboxes, there will be greater opportunity for millimeter-scale robot designs due to the wireless nature and high torque density of the magnetic actuators compared with other miniature rotary actuators (fig. S1).

Here, we propose a series of millimeter-scale magnetically actuated gearboxes with a mass as little as 13.2 mg, a maximum size of 3 mm, and a reduction ratio of up to 342 for robots at the millimeter scale. It can produce 0.182 mNm of output torque and 0.134 mW of output power at a 40-Hz rotating magnetic field with a strength of less than 6.8 mT. In combination with different functional modules, the gearbox can be driven wirelessly to repeatedly generate large actuation forces, strains, and speeds; store energy in elastic components; and lock up mechanical linkages. The robots developed based on this gearbox can achieve peristaltic crawling, jumping locomotion, and various solid and liquid sampling functions at the millimeter scale (Movie 1).

RESULTS

Miniature gearbox for wirelessly driven magnetic actuation

We considered a gearbox design that can fit magnetic actuators and realize rotary motion under an external rotating magnetic field (**B** field) (Fig. 1A). The design of the gearbox is described in the "Gearbox design" section. This parallel-shaft gear train design consists of five components: gears, sleeves, shafts, plates, and a ferromagnetic disk. Seven gears are contained in a gearbox with dimensions of 2.5 mm by 3 mm by 1.5 mm (excluding the magnetic disk) to generate a reduction ratio of 342. The design parameters of all gears are given in table S1. The input and output gears are single gears (blue in Fig. 1A) fixed to the input and output shafts, respectively. Other gears are duplex gears (gray in Fig. 1A) that can slide and rotate freely on the shaft. The magnetic disk is fixed to the input shaft to power the gearbox. The axial locations of the gears are constrained by sleeves to avoid disengagement or interference. When an external rotating magnetic field **B** was applied, the magnetic disk could rotate along with the rotating **B** and produce input torque to the gearbox. The gear train amplified the input torque and drove the load with the output shaft. The rotational direction of the output shaft could be controlled by changing the direction of the rotating **B**. All parts of the gearbox were fabricated by a two-photon polymerization–based three-dimensional (3D) microprinting system (Photonic Professional GT, Nanoscribe GmbH) or casting (Fig. 1B), as detailed in the "Fabrication of the miniature gearboxes" section. This approach allows submillimeter-sized gears to be fabricated (Fig. 1C and fig. S2).

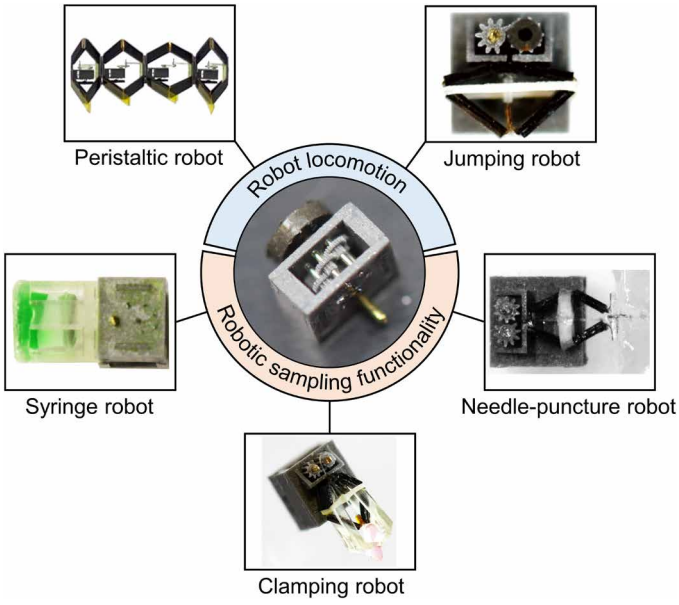

Movie 1. Overview of the magnetically actuated gearbox for various robot locomotion and robotic sampling functionalities at the millimeter scale.

The performance of the gearbox was tested through weight-lifting experiments. In these experiments, the rotating **B** was generated by a cylindrical Halbach array (Fig. 1D, fig. S3, and movie S1), as detailed in the "Magnetic actuation setups" section. The magnetic field strength was tuned by adjusting the distance between the gearbox and the Halbach array. Weights to be lifted were attached to the output shaft through a thread. The displacement of the weights was constrained by a guide rail so that the weights could only move vertically. The time-varying input magnetic torque was calculated by measuring the angle between the magnetization direction of the magnetic disk and the external **B** from the images captured by a high-speed camera (fig. S4). To drive the gearbox in air, a minimum $|\mathbf{B}|$ of 0.2 mT was required even if there was no weight attached to the output shaft. The frictional properties of the gear tooth surfaces, the fidelity of the gear geometry, the mesh stiffness of the gears, and the positioning error of the shaft during the assembly process are all possible factors that can induce such nonzero $|\mathbf{B}|$. When lifting a 103.2-g weight using a 40-Hz rotating **B** with a strength of 6.8 mT, the tiny gearbox produced an output torque of 0.182 mNm and an output power of 0.134 mW, which corresponds to a torque density of 12.15 $\mu Nm/mm^3$ and a power density of 8.93 $\mu W/mm^3$. We further calculated the input magnetic torque to be 1.85 μNm, the input power to be 0.465 mW, and the transmission efficiency to be 28.8% (detailed in the "Gearbox performance characterization" section). Further increasing the weight can potentially damage the gear teeth. Using materials with a higher strength to fabricate the gearbox components could increase the maximum output torque of the gearbox (*31*), which will be investigated in the future. The gearbox also endows the magnetic actuator with self-locking capability. Without the external magnetic field, the gearbox can withstand a load torque of up to 0.13 mNm acting on the output shaft. A larger load torque would lead to backdriving of the gearbox.

The transmission efficiency of the gearbox at different actuation frequencies is shown in Fig. 1E. The gearbox efficiency was around 27% in the air and decreased when the gearbox was submerged in water and water-glycerol solution. Other performance metrics, including input magnetic power, output mechanical power, torque density, and power density, are presented in fig. S5. The transmission efficiency did not vary significantly with the changing actuation frequency in the air [$P = 0.07$, analysis of variance (ANOVA)] and water ($P = 0.21$, ANOVA). However, it decreased with the

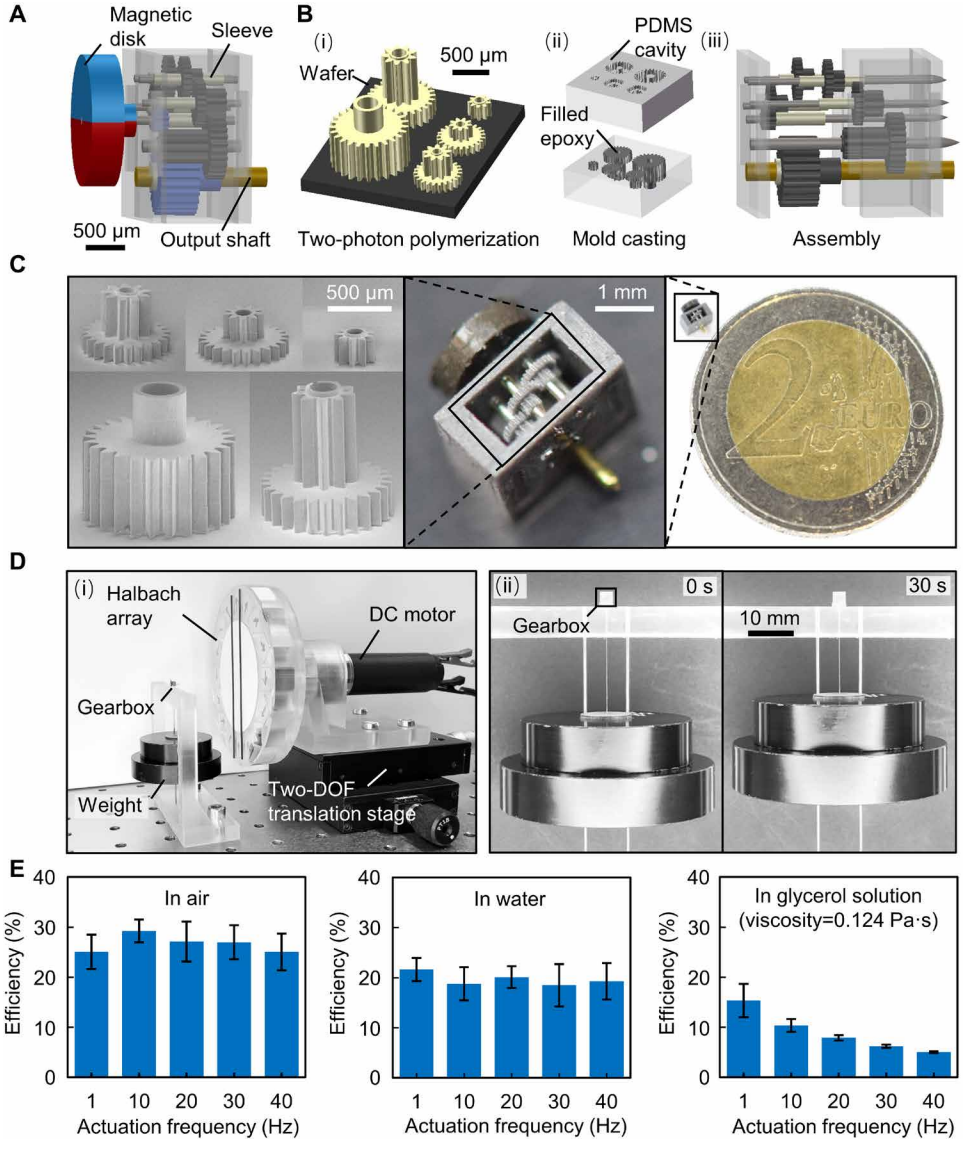

Fig. 1. Design and performance of the magnetically actuated miniature gearbox for millimeter-scale magnetic actuators. (**A**) Design of the miniature gearbox with a reduction ratio of 342. A magnetic disk is fixed to the input shaft, which can be driven by a rotating magnetic field. (**B**) Fabrication process of the gearbox. The components of the gearbox were fabricated by casting, except for the shafts made of metal rods. (**C**) Scanning electron microscope images of the fabricated gears and photos of the assembled gearbox. (**D**) Characterization setup of the gearbox. (i) The load was adjusted by changing the weights attached to the output shaft. The strength of the magnetic field generated can be adjusted by tuning the distance between the gearbox and the Halbach array. (ii) Lifting weight under a 40-Hz **B** field. (**E**) Characterization of gearbox efficiency for lifting 23.2-g weights in air, water, and water-glycerol solution at different actuation frequencies. Error bars represent SD ($N = 10$).

increasing actuation frequency in a high-viscosity water-glycerol solution ($\eta = 0.12355$ Pa·s) largely due to the fluid drag torque acting on the fast-rotating magnetic disk. The simulation revealed that the fluid drag torque could reach 1.45 μNm in water-glycerol solution at a 40-Hz rotating **B**, which was 20 times higher than the torque measured in water (fig. S6). Another possible factor that caused lower transmission efficiency in liquids than in the air was the small air bubbles that were inevitably trapped in small gaps. These bubbles can induce capillary forces that impede the motion of the movable parts (*32*).

We used simulation to evaluate the influence of the friction between different gearbox components (detailed in the "Numerical simulations" section). To validate the simulation model, we conducted the weight-lifting experiments with the gear pair configuration shown in Fig. 2Ai and table S1. It shared the same experimental setup as the gearbox characterization. A 1-Hz rotating **B** was applied to lift different weights attached to the output shaft. The mean input torques and the transmission efficiencies obtained at different output torques and gear materials are reported in Fig. 2A. The friction coefficients of different gear materials were determined experimentally (fig. S7), as detailed in the "Friction coefficient measurements" section. The input torque required by the gearbox was positively correlated to the output torque, as demonstrated by both simulations and experiments in Fig. 2Ai. However, the experimental data were lower than the simulated ones by 0.31 to 0.36 μNm for the aluminum-filled epoxy resin (EpoxAcast 655, Smooth-On) and 0.23 to 0.33 μNm for the negative-tone photoresist (IP-S, Nanoscribe GmbH). The transmission efficiencies obtained in experiments were also lower than the simulated ones by 5.6 to 10.1% for EpoxAcast 655 and by 1.7 to 7.6% for IP-S photoresist. The variation of the simulated transmission efficiency at different output torques was unnoticeable, whereas the transmission efficiency calculated from the experiments gradually increased and approached the simulated value with increasing output torque. In our simulation, we did not include the influence of the friction between the weights and the guide rail and between the gears and the gearbox side plates. These frictions contributed to the discrepancies between experimental and simulated data.

With this simulation model, we considered two spur gears with a module of 0.03 and teeth numbers of 9 and 23 (fig. S8). The frictions between the gear teeth and between the shafts and the holes were considered to be Coulomb friction with friction coefficients μ_1 and μ_2, respectively. The friction between the shaft and the hole had a more adverse influence on transmission efficiency than the friction between the gear teeth. This can be seen in Fig. 2B, where the transmission efficiency dropped by around 11% if μ_2 was fixed and μ_1 was increased from 0 to 0.5, whereas it dropped by around 25% if μ_1 was fixed and μ_2 was increased from 0 to 0.5. In addition, the friction between the gear teeth also influenced the gear mesh force (F) and root mean square deviation (RMSD)

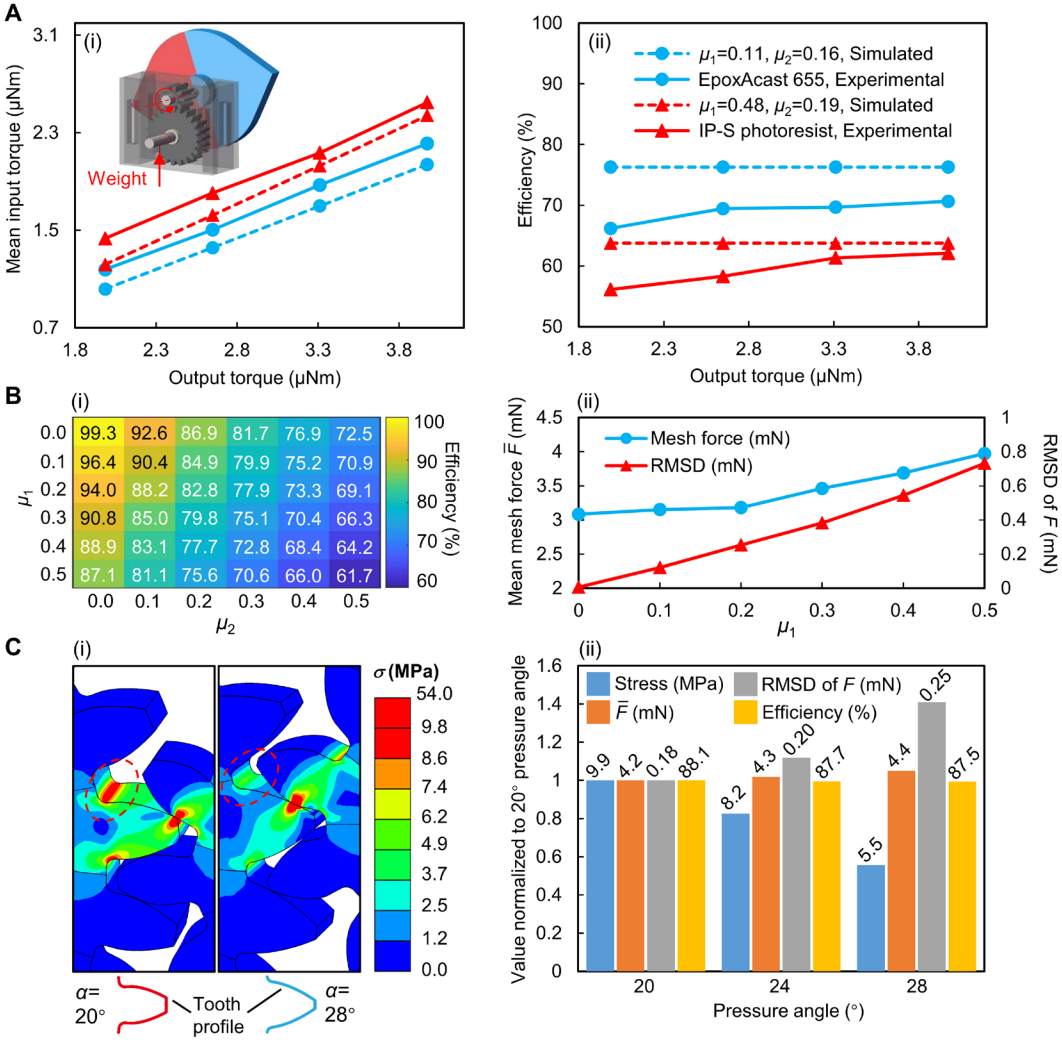

Fig. 2. Simulation analysis of the meshing gear pair. (**A**) Benchmark validation. Comparison of simulated and experimental (i) mean input torque and (ii) transmission efficiency with different materials and loads. The friction coefficient between the gear teeth is μ_1. The friction coefficient between the shaft and the hole is μ_2. (**B**) Simulation analysis of different friction coefficients on gearbox performances. (i) Influence of the friction coefficients on the transmission efficiency. (ii) Influence of the friction coefficients on the mean value and RMSD of the time-history resultant mesh force *F*. (**C**) Influence of the pressure angle on (i) maximum bending stress at the tension side of the tooth root and (ii) other transmission performance metrics. μ_1 and μ_2 were set to 0.11 and 0.16, respectively.

of *F* (Fig. 2B). RMSD of *F* represents the degree of mesh force oscillation that can lead to gearbox vibration and shock loads. As μ_1 increased from 0.1 to 0.5, the mean value of *F* ($\bar{F}$) increased from 3.15 to 3.97 mN (increased by 26%), and the RMSD of *F* increased from 0.12 to 0.73 mN (increased by 508%). To reduce the friction between the shaft and the holes, we designed the diameters of the holes on the gears to be slightly larger than the diameters of the shafts. The aluminum-filled epoxy resin we used to fabricate the gears has a low friction coefficient (fig. S7), which is favorable for decreasing the friction between the gear teeth.

The most commonly observed failure mode of the gearbox during the experiment was the fracture of the gear teeth root. One possible solution to this issue was to increase the pressure angle. In the first version of the gear design, the pressure angle was selected as 20°, which is widely adopted in the industry. Such a pressure angle only achieved a maximum output torque of 0.113 mNm. By increasing the pressure angle to 28°, we achieved a maximum output torque of 0.182 mNm without damaging the gears. The simulation revealed that a large pressure angle can decrease the maximum bending stress at the tension side of the tooth root by 44% (Fig. 2C), enhancing the load capacity of the gearbox. Increasing the pressure angle from 20° to 28° only caused a slight reduction (0.7%) in transmission efficiency and a slight increase in *F* (5%). However, the RMSD of *F* was noticeably increased by 39% (Fig. 2C). In the following, we applied a pressure angle of 28° to the gearboxes of the jumping and the peristaltic robots to increase their load capacity. The pressure angles of the gearboxes used in various sampling robots were set to be 20° to decrease the undesired vibrations. Apart from the pressure angle, increasing the module of a given gear is another possible solution to increase the gear strength. The larger the module, the greater the teeth root width and the higher the torque can be transmitted (*33*). We have discussed the rationale of the gear module selection in the "Gearbox design" section.

Peristaltic robot controlled by the wireless gearbox

The magnetically actuated miniature gearbox can enable locomotion modes that could not be achieved in previous wireless millirobots. One typical example is the earthworm-inspired peristaltic locomotion. Peristaltic locomotion has been achieved in previous studies through many different approaches. At centimeter or larger scales, it has been realized by using heterogeneous magnetic fields (*34*), pneumatic actuators (*35*, *36*), electrical motors (*37*–*40*), electromagnetic actuators (*41*), and shape memory alloy actuators (*42*). However, scaling down these designs to millimeter or even smaller scales to realize mobile wireless robots is very challenging. For robots driven by heterogeneous magnetic fields, the challenge comes from the difficulties of realizing spatially heterogeneous **B** field at high spatial resolution. Robots driven by electrical motors, pneumatic actuators, electromagnetic actuators, and shape memory alloy actuators require onboard power sources, electrical wires, and air lines, whereas miniature robots have limited onboard spaces and a wireless actuation strategy is preferred. At millimeter or smaller

scales, peristaltic motions were achieved through hydrogel (*43*, *44*) or liquid-crystal elastomer (*45*) actuators. To drive these robots, we used scanning laser beams to heat up the material in a scanning manner to produce the traveling peristaltic wave. This actuation strategy has two drawbacks. First, the light-driven robots are still tethered by the light beam, which prevents the robots from functioning in environments that are not transparent to the given light wavelength. Second, the actuation speed by heating is capped by the heating and cooling rates, leading to slow locomotion speeds. For millirobots that are controlled by the uniform magnetic field, periodically producing such wave-like body contraction and expansion becomes even more challenging because the adjacent body segments have to respond to the same control input differently. In this regard, we demonstrate that by using the gearbox, an earthworm-inspired peristaltic millirobot can be developed.

The proposed robot has four segments, and each of them can contract and expand rhythmically under the external rotating **B** to propagate a peristaltic wave along the robot body. The body frame of each segment is a four-sided Sarrus linkage that can produce circular expansion or contraction through linear motion (*46*). To drive this linear motion, we used a two-bar linkage to connect the output shaft of the gearbox and one end of the Sarrus linkage, as shown in Fig. 3Ai. The rotating **B** rhythmically changed the angle θ (Fig. 3Aii), causing the contraction and expansion of each body segment. The Sarrus linkage fabrication and segment assembly are described in the "Fabrication of the functional modules" section and Fig. 3B. The robot frame was fully contracted when θ was 0°. At this state, the lengths of axes 1 and 2 were 4.4 and 11.7 mm, respectively (Fig. 3Biii). As θ increased, the length of the axis 1 increased, and the length of axis 2 decreased. The full expansion of the frame was reached at θ = 180°. At this state, the lengths of axes 1 and 2 were 7.8 and 8.4 mm, respectively. The segment completed an expansion/contraction cycle when θ varied from 0° to 360°.

To transmit a steady peristaltic wave along the body, we connected four segments end to end with a 90° initial phase difference between the adjacent segments, as shown in Fig. 3Aii. The initial θ from the first segment to the fourth segment was 0° (360°), 270°, 180°, and 90°, respectively. When a global rotating **B** was applied, the gearboxes drove their output links at the same speed. Hence, the phase differences between adjacent segments were maintained, and a traveling wave along the robot length was created. The length of the robot remained almost constant during the actuation, when the difference of the initial θ between the two adjacent segments was 90°.

The locomotion capability of the peristaltic robot was first tested on a flat Dragon Skin 10 substrate (Fig. 3Ci and movie S2). A 33-Hz rotating **B** in the plane parallel to the substrate was produced by two antisymmetrically placed permanent magnets (detailed in the "Magnetic actuation setups" section; fig. S3C). The maximum $|\mathbf{B}|$ measured at the center of the substrate was approximately 15 mT. To increase the friction between the robot and the substrate, we attached four pairs of insect feet–like polyimide slices to the robot body. Under the above experimental conditions, the robot moved 68.7 mm on the substrate in 132 s at an average speed of 0.52 mm/s. The phase difference between the adjacent segments was constant before and after the locomotion, indicating that all gearboxes functioned properly. During the locomotion, the friction between the robot and the substrate restricted most of the body rotation due to the rotating **B**. A yawing angle of only 12.5° was observed during the 132-s locomotion (fig. S9Ai). Subsequently, the robot was tested in a glass tube with an inner diameter of 13 mm (Fig. 3Cii, fig. S9Aii, and movie S2). Under this test condition, the four pairs of robotic feet were no longer needed and were removed from the body frame. By applying the same **B** as used in the movement on the flat substrate, the robot moved 81.5 mm in 120 s at an average speed of 0.68 mm/s, which is faster than on the flat substrate. One possible reason is that the existence of the tube wall confined the robot locomotion in one dimension, eliminating the body rotation and increasing the resultant speed.

The forward locomotion of the robot was generated by alternately anchoring to the substrate and elongating the body. For illustration, the head displacement of each segment and the corresponding segment expansion/contraction states are plotted in Fig. 3Di. To achieve the forward movement of one segment, the following two requirements have to be satisfied. First, this forward-moving segment is expanding. Second, at least one other segment is anchored to the substrate. We take the forward movement of segment 1 as an example (from point a to b in Fig. 3Di). During this period, θ of segment 1 varied from 90° to 180°, and segments 2 and 3 were anchored to the substrate. It was evident that segment 1 contracted as θ varied from 180° to 360°, which caused a slight decrease in displacement (point b to c in Fig. 3Di). The robot used a similar mechanism to move inside a tube, which can be verified by fig. S10. The crawling speed of the robot can be controlled by varying the actuation frequency of the external magnetic field (fig. S9B and movie S3). The crawling speeds measured on a flat substrate and inside a glass tube are presented in Fig. 3Dii. The fastest crawling speed achieved on the robot was 0.10 body length (BL)/s on the flat substrate and 0.12 BL/s inside the glass tube. The fastest peristaltic robot reported in previous studies was made of dielectric elastomer actuators (*47*), which can achieve a crawling speed up to 1.19 BL/s, exceeding our robot. However, this robot is tethered and requires a very high actuation voltage of up to 2 kV. Our peristaltic robot is still among the fastest being reported and is the fastest untethered peristaltic robot among them (fig. S11).

Jumping robot controlled by the wireless gearbox

The challenge of realizing high-performance jumping is to reduce the size and mass of the robot as much as possible while still being able to store large mechanical energy, hold back the mechanism being preloaded, and trigger the energy release quickly. Inspired by miniature jumping insects such as fleas and froghoppers (*48*), we proposed a millimeter-scale (3.1 mm by 2.9 mm by 3.1 mm) jumping robot that has a parallel-elastic leg (*49*–*51*) (Fig. 4A). Specifically, the robot leg is a five-bar linkage that is connected in parallel with a latex spring. By pulling the thread connected to the foot, the leg is retracted, and the spring is elongated. By loosening the thread after the leg is fully retracted, the elastic energy stored in the spring is released to extend the leg rapidly. The motion of pulling and loosening is realized by a pair of gears, one of which has two missing teeth (gear 1 in Fig. 4Ai) and is fixed to the output shaft. The thread is attached to another gear that has complete teeth (gear 2 in Fig. 4Ai). When these two gears engage normally, gear 2 will pull the thread to retract the leg or hold the leg at the current position, and gear 1 will serve as a latch (folded state). If the tooth that is going to mesh is missing, gear 2 will suddenly release the thread and rotate freely (relaxed state).

This jumping mechanism allows the robot to jump repeatedly. For demonstration, the robot was placed inside a box with a 2-mm-thick soft substrate (Dragon Skin 10, Smooth-On). By applying appropriate

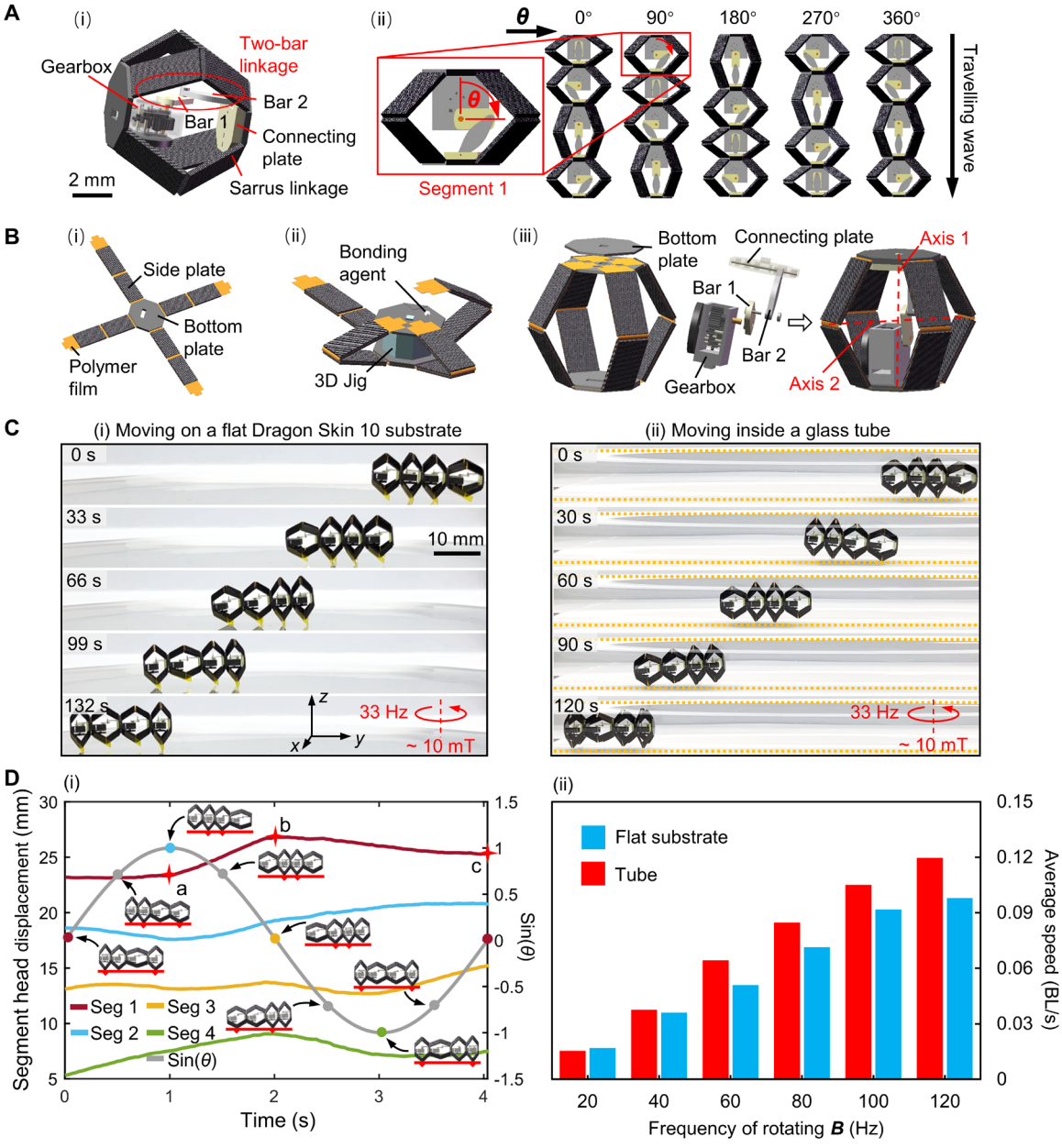

Fig. 3. Miniature untethered peristaltic millirobot with earthworm-like locomotion. (**A**) Design of the robot with four segments using a magnetically actuated gearbox in each segment and external magnetic actuation. (i) A Sarrus linkage is used as the frame for each segment. The magnetically actuated gearbox combined with a two-bar linkage is used to drive the frame for earthworm-like contraction and expansion. (ii) The phase difference of bar 1 between adjacent segments is 90°. The robot can transport a traveling wave along the body under a rotating **B**. (**B**) Assembly process of a robot segment. (i) An unfolded Sarrus linkage was fabricated. (ii) A 3D jig was used to assist the folding and joint bonding of the Sarrus linkage. (iii) A gearbox assembled with a two-bar linkage was plugged into the Sarrus linkage to form the final segment. (**C**) Side views of the peristaltic locomotion. (i) The robot with feet attached to the frame can move on a flat Dragon Skin 10 substrate. (ii) The robot can move inside a glass tube without additional feet. The yellow dotted lines indicate the inner profile of the glass tube. (**D**) Locomotion analysis. (i) Displacement of each segment and the variation of sin(θ) of segment 1 during one period of the peristaltic locomotion. (ii) Locomotion speed characterization under different actuation frequencies.

external magnetic fields at different stages, the robot was able to complete one jumping cycle—including the attitude adjustment before energy storage, the energy storage, the attitude adjustment before triggering, and the final trigger of the jumping—as shown in fig. S12 and movie S4. Note that the robot was able to keep the spring stretched even when the external magnetic field was removed because the reduction ratio of the gearbox was high enough (342) that the internal friction was sufficient to prevent the reverse rotation of the gears. We performed 11 consecutive jumps back and forth in a repeated jumping experiment to test the reliability of the gearbox and the jumping mechanism (Fig. 4Bi and movie S4). The heights and the horizontal distances of nine jumps that did not hit the wall were examined (Fig. 4Bi), and we found that the jumping performance of the robot was stable.

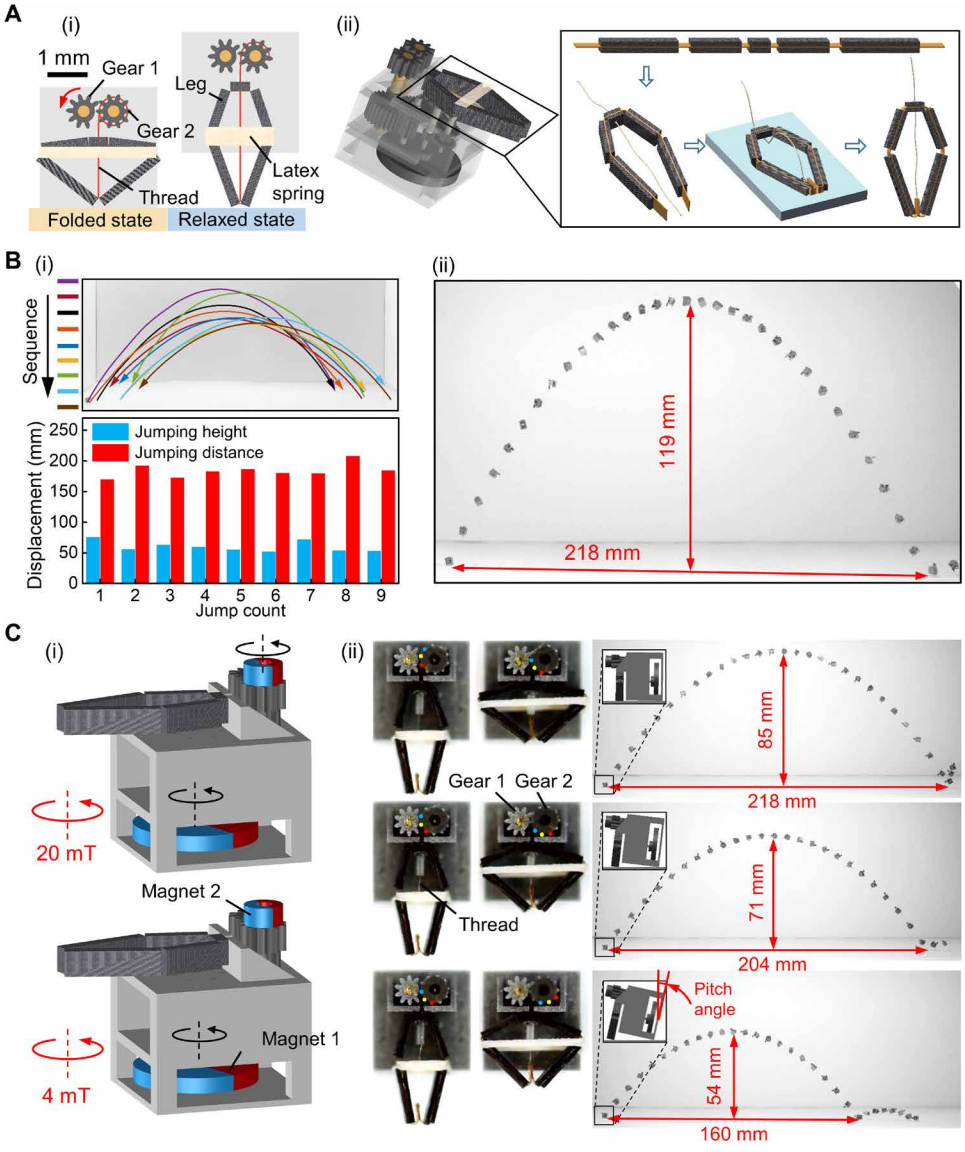

Fig. 4. Miniature untethered jumping robot. (**A**) Design of a miniature jumping robot using the proposed gearbox and magnetic actuation. (i) Design of the jumping mechanism. A latex spring is connected in parallel with the five-bar leg. The gearbox drives a gear with two missing teeth (gear 1) for energy storage and jumping motion triggering. (ii) Fabrication of the leg linkage. First, the open-chained linkage was fabricated. Then, the bonding agent was applied to the foot joint to close the chain. The bonding process was conducted in a jig. (**B**) Performance characterization of the robot. (i) Repeatable jumping experiments on a soft substrate. Of the 11 consecutive jumps, the jumping heights and the jumping distances of the 9 jumps that did not hit the wall were counted. (ii) Jumping process of the robot on a rigid substrate when equipped the stiffest spring. The image was obtained by stacking the image sequence with a 10-ms time interval. (**C**) Wireless jumping height modulation. A magnet (magnet 2) with a lower remnant magnetization is attached to the gear for thread winding (gear 2) to control the stored elastic energy and leg state before the jump triggering. As the stored energy decreased and the pitch angle increased before the triggering, the jumping height decreased.

To push the limit of the jumping performance, the robot was equipped with a very stiff latex spring and jumped on a rigid substrate. After triggering, the 25.2-mg robot was able to rapidly extend its leg in 0.75 ms and reach a takeoff speed of 2.3 m/s, acquiring a kinetic energy of 0.067 mJ. It achieved a jumping height of up to 119 mm (38.4 BL) and a horizontal displacement of up to 218 mm (70.3 BL) (Fig. 4Bii and movie S4). The notable horizontal displacement can be achieved because we offset the plane of the leg linkage from the centroid of the robot body. The jumping height of the robot surpasses other millimeter-scale jumping robots developed in previous studies, except for the one reported in (*52*), where a jumping height of 75 BL was achieved (fig. S13). To trigger the jumping, a near-infrared (NIR) laser source of up to 2.34 W has to be precisely placed close to the spherical hydrogel actuator (4 to 35 mm) to locally heat a 0.28-mm^2 area of the actuator's bottom part to 126°C. As a result, the jumping height and direction are very sensitive to the spot position, inducing challenges in motion control. In comparison, the magnetic jumping robot allows the magnetic source to be placed far away and can work in nontransparent environments that NIR or other light sources cannot penetrate.

The jumping height of the robot can also be tuned by external magnetic field (Fig. 4C and movie S5). To adjust the jumping height, we made a slight modification to the gearbox by attaching a small magnet to gear 2 (magnet 2 in Fig. 4Ci). This small magnet has a lower remnant magnetization than the magnetic disk (magnet 1) attached to the input shaft of the gearbox. Therefore, it requires a stronger **B** field to rotate. Figure 4Cii demonstrates how we can use these two magnets with different remnant magnetizations to adjust the elastic energy stored in the spring. At the relaxed state, gear 2 can rotate freely (Fig. 4Cii). By applying a strong rotating **B** field, we can control the rotation of gear 2 to control which gear tooth is going to be engaged. The rotating **B** field can also rotate magnet 1 at the same time. However, because of the large reduction ratio, gear 1 can only rotate slightly and still allow gear 2 to freely rotate. We then applied a weaker rotating **B** field to only rotate magnet 1 while keeping the magnet 2 at rest. Gear 1 then engaged gear 2 at the chosen tooth and finally folded the leg linkage to the desired state. This strategy can control the retraction stroke of the leg and change the energy stored in the spring and the body pitch angle, resulting in different jumping heights (Fig. 4Cii).

Solid and liquid sampling robots controlled by the wireless gearbox

Some robotic tasks, such as fine-needle biopsy (*25*, *53*), can also benefit from energy storage and triggering mechanisms for power

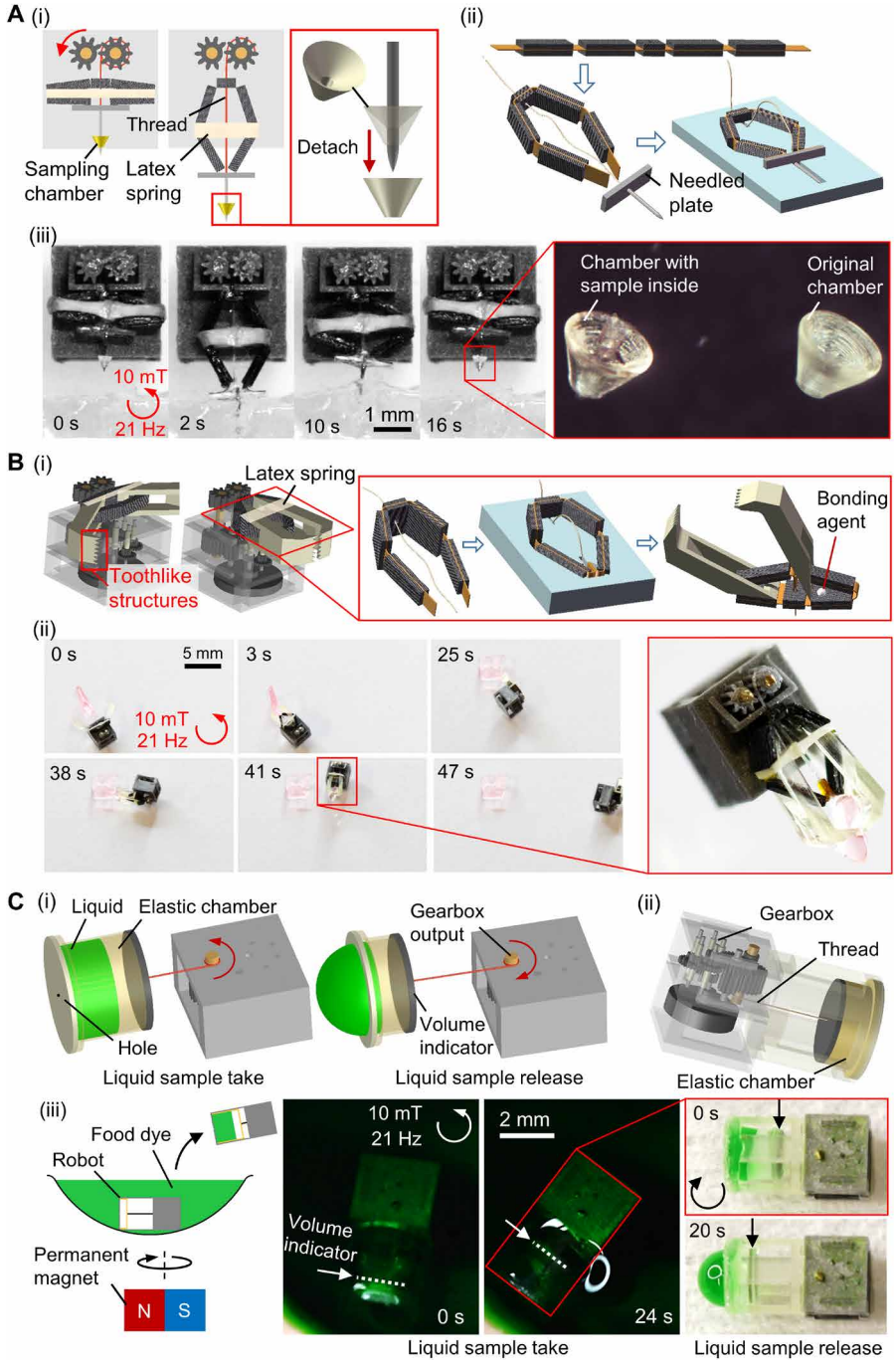

Fig. 5. Untethered millimeter-scale sampling robots. (**A**) Needle-puncture robot for sampling from inside of solid objects. (i) By attaching a needle to the parallel-elastic folding mechanism, repeatable puncture and retraction can be achieved. The sampling chamber mounted to the needle tip can collect samples during the needle retraction. (ii) Fabrication process of the parallel-elastic folding mechanism with the needle. (iii) After conducting puncture and retraction three times, the samples were collected in the sampling chamber, which can be observed under an optical microscope. (**B**) Clamping robot for sampling from the surface of the solid objects. (i) By integrating a clamp to the parallel-elastic folding mechanism, repeatable clamping and opening can be achieved. (ii) After the robot quickly pinched the gel, the robot was dragged by the magnetic field to tear off a piece of gel. (**C**) Syringe robot for imbibing and ejecting liquid samples. (i) To imbibe the liquid into the chamber, the gearbox stretched the elastic reservoir by pulling the thread. To release the liquid, the output shaft rotated to another direction and let the elastic reservoir restore its original volume. (ii) Mechanical design of the robot. (iii) The robot was placed in a puddle of colored liquid to take samples by applying a rotating **B** counterclockwise. Under a rotating **B** in the opposite direction, the robot released the samples inside.

amplification. Here, we demonstrate a needle-puncture robot that can pierce into an object and obtain samples by retracting the needle (Fig. 5Ai). Similar to the jumping mechanism in Fig. 4A, a six-bar linkage was used to provide large strokes for the needle piercing and retraction motions. A needle with a sampling chamber was fixed to the end bar of the six-bar linkage. The detachable sampling chamber has a hollow structure to collect samples during needle retraction. The chamber was located above the needle tip to facilitate the needle piercing.

To demonstrate its functionality, we placed the robot on an elastomeric polydimethylsiloxane (PDMS) substrate, and placed a piece of gel in front of it as the target. A single permanent magnet was used to drive the robot (detailed in the "Magnetic actuation setups" section). It can generate a gradient force on the magnetic disk and pull the robot toward the substrate, increasing the friction between the robot and the substrate to restrain undesired body movement during the sampling. The sampling process consisted of two stages (Fig. 5Aiii and movie S6). In the first stage, the robot with prestored energy shot the needle under a rotating **B**. The needle carrying the sampling chamber pierced into the gel. In the second stage, the robot retracted the needle from the gel. After three cycles of needle puncture and retraction, visible samples can be found in the sampling chamber.

The energy storage and triggering principles used in the needle-puncture robot can also be used to design a clamping robot to sample objects by grasping (Fig. 5Bi). The clamp was designed with tooth-like structures with the aim of firmly gripping the sample when the clamp was closed. After triggering the mechanism, the clamps rapidly closed and pinched the gel in front of it (Fig. 5Bii and movie S7). By applying a magnetic field to pull and rotate the robot, a small piece of sample can be removed from the bulk gel.

Apart from the solid object sampling, the gearbox was also used to develop a syringe robot that can collect liquid samples, such as liquid biopsy (*54*, *55*), or release liquid content, such as an active drug (*56*), from the elastic reservoir (Fig. 5C). The reservoir for storing the

liquid was an elastic chamber with two plates at each end (Fig. 5Ci). One of the plates had a 40-μm-diameter opening in the center to let the liquid flow through. Another plate, which also works as a liquid volume indicator, was pulled through a thread connected to the output shaft of the gearbox. The output shaft could rotate counterclockwise to imbibe the fluids by stretching the elastic reservoir or rotate clockwise to release the liquid content by letting the elastic reservoir return to its unstretched state. The elastic reservoir could be stretched from 1.1 to 2.8 mm, corresponding to a volume change of 6.2 mm^3. The amount of liquid being imbibed or released could be modulated by controlling the stretched length of the reservoir. The reservoir could hold liquid contents inside when the external magnetic field was turned off. The liquid sampling and releasing capabilities are demonstrated in Fig. 5Ciii and movie S8.

DISCUSSION

In this study, we demonstrate how a magnetically actuated miniature gearbox can be used to generate force amplification on wireless millimeter-scale robots. The gearbox can be driven by a rotating external magnetic field of no more than 6.8 mT to produce an output torque of up to 0.182 mNm and a torque density of up to 12.15 μNm/mm^3. The torque density of the overall gearbox (including the magnetic disk) driven by a 6.8-mT magnetic field is greater than the that of magnetic actuator driven by a 40-mT magnetic field (fig. S1). The large reduction ratio of the gearbox guarantees a large output force and reduces the requirements to the strength of the magnetic field, which helps suppress the rigid-body rotation due to the magnetic torque (*4*). However, the benefits of the large reduction ratio come at the expense of a slow output rotational speed, which is a trade-off in reduction ratio selection. The gearbox is steerable, which can be achieved by applying a magnetic pulling force or a magnetic torque. With the combination of the gearbox and the functional modules, we achieved stable peristaltic crawling with a speed up to 0.12 BL/s; repeatable, steerable, and height-adjustable jumping with a maximum jumping height of 38.4 BL and a maximum jumping distance of 70.3 BL; and various functional robots that can collect solid and liquid samples.

By redesigning the input shaft of the gearbox using magnetic components, the gearbox can be adapted to actuators with other motion types, such as linear and bending motions, which are typical in small-scale actuators (fig. S14 and movie S9) (*57*, *58*). In addition to force amplification, transforming the linear and bending motions to rotary motion can also eliminate the limitations of the work that can be done within an actuator's single stroke through work multiplication (*59*). We envisage that the magnetically actuated miniature gearbox can greatly broaden the design space and enhance the locomotion performance and functions of millimeter-scale robots driven by different types of miniature actuators.

Several challenges still need to be overcome to develop the next-generation magnetically actuated miniature gearbox. First, the maximum output torque and the torque density of the gearbox are limited by the material strength of the aluminum-filled epoxy. Using materials with higher strengths to fabricate gears will increase the load capacity of the gearbox. Second, the gear train inside the gearbox is open to the outside space, which makes it vulnerable to small particles from the surrounding environments. The small particles can stick to the surface of the gear teeth, deteriorating the gear meshing quality. A protective shield is required to isolate the gear train from the surrounding environments so that the gearbox can also function properly with the existence of small particles, such as dust. Third, the fabrication of the gearbox requires a manual assembly process, which lowers the fabrication efficiency. Manufacturing devices, such as micromanipulators, are promising to speed up this assembly process.

MATERIALS AND METHODS

Gearbox design

The multistage parallel-shaft gearing systems were chosen as speed reducers for magnetic actuators because of their compact size and ease of assembly. The overall reduction ratio of the gearbox was determined by the output torques required in different robotic applications. In the cases of the jumping robot and the clamping robot, the gearbox was designed to have a reduction ratio of 342 so that the gearbox can output a large enough torque to store elastic energy in the parallel-elastic linkage. Another advantage of adopting a large reduction ratio is that the gearbox can be driven by a small magnetic field, alleviating the robot body rotation because of the magnetic torque. However, a large reduction ratio decreases the rotational speed of the output shaft. Hence, in the peristaltic robot, we decreased the reduction ratio to 134 to increase the crawling speed.

The reduction ratio of each gear stage is usually restricted to 5 or less. The gearboxes of some commercial electromotors even restrict the reduction ratio between 2.2 and 3.6 (*31*). The selection of an overly large single-stage reduction ratio would decrease the compactness of the gear train. To realize a compact gearbox design (the maximum size was limited to 3 mm), we limited the reduction ratio of each gear stage between 2.5 and 3, following the design conventions. The reduction ratio of each gear stage is determined by the reference diameters of the two gears at that stage. The reference diameters of the gears were selected to ensure that the gearbox's maximum size was smaller than 3 mm.

When the reference diameter of the gear is determined, the number of teeth is solely determined by the gear module: the larger the gear module, the smaller the teeth number. Selecting a large gear module can decrease the bending stress at the gear tooth root. However, a large gear module also decreases the teeth number, decreasing the transmission accuracy. In our case, the gear strength is the utmost factor we need to consider, so we chose a relatively large gear module for the gear design (0.03 to 0.045 mm). In the meantime, we also need to make sure that the teeth numbers of the two gears at each gear stage are prime to each other to ensure uniform wear. With the above requirements, we selected the gear module and teeth number in table S1.

There are two guidelines we followed to design the gear thickness. First, one of the gears of a gear pair needs to have a larger thickness than the other to ensure proper meshing. In our design, the driving of the gear pair was thickened. Second, the gear that is easily broken needs to be thickened.

The length, width, and height of the final gearbox design are 3, 2.5, and 1.5 mm, respectively. To guarantee the fabrication quality of the gear, the minimum gear thickness was restricted to 125 μm, and the minimum outside diameter was restricted to 336 μm (table S1).

Fabrication of the miniature gearboxes

Gears and plates were fabricated by casting. Positive molds were first fabricated on silicon wafers using two-photon polymerization with the negative-tone photoresist (IP-S, Nanoscribe GmbH). These

positive molds were then silanized with trichloro(1*H*,1*H*,2*H*,2*H*-perfluorooctyl) silane 97% (Merck KGaA) for ease of demolding. PDMS (Sylgard 184, Dow Corning; mixing precursor and curing agent at 10:1 mass ratio) was cast onto the positive molds and cured at 90°C for 1 hour to create the negative molds. After curing, the positive molds were carefully taken out from the PDMS negative molds immersed in ethanol using a tweezer. An aluminum-filled epoxy resin (EpoxAcast 655, Smooth-On) was cast into the silanized negative molds and then vacuum degassed to remove the trapped gases. The excess resin was removed via a razor blade. After curing at 23°C for 12 hours and heat curing at 80°C for 3 hours, the parts were taken out using a tweezer.

The magnetic disk was also fabricated using a similar molding method. The material used for casting was a mixture of uncured PDMS (the mass ratio of precursor and curing agent is 10:1) and NdFeB magnetic particles (MQP-15-7, Magnequench; average diameter, 5 μm), with a mass ratio of 1:4. After curing, the magnetic disks were magnetized along the diameter direction using a vibrating sample magnetometer (VSM; EZ7, MicroSense). The machine can generate a strong uniform magnetic field of 1.8 T, resulting in magnetization of 338 kA/m.

Brass rods (BW03, Albion Alloys) and acupuncture needles (S-J2030, S-J1215, and S-J1415, Seirin Corporation) with different diameters (0.3, 0.2, 0.12, and 0.14 mm) were used as shafts for the gearbox. The sleeves fabricated through two-photon polymerization were used to confine the gears to the designed locations. The gears and the corresponding sleeves did not need to be fixed to the rods except for the gears on the input and output shafts (Fig. 1A). We used dimethacrylate adhesive (Loctite 601) to fix the gears to the shaft. The magnetic disk also needed to be fixed to the input shaft via the cyanoacrylate adhesive (Loctite 495). The assembly process was conducted under a stereomicroscope (ZEISS Stemi 508, Carl Zeiss Microscopy GmbH). After the assembly, the extra parts of the shafts outside the gearbox were cut away with a laser cutter (LPKF ProtoLaser U3).

Fabrication of the functional modules

Linkages were used in functional modules to transform the rotational motion into other motion forms. The linkage with rigid links and flexure joints were fabricated to develop the Sarrus linkage in the peristaltic robot (Fig. 3B) and the five-bar linkages in the jumping robot, needle sampling robot, and clamping robot (Figs. 4Aii and 5, Aii and Bi). As a typical example, the fabrication of the Sarrus linkage shown in Fig. 3B is described below. This linkage consists of 2 bottom plates, 16 side plates, and a polymer film. The bottom plate with the rectangular hole in the middle was fabricated using the casting method described in the "Fabrication of the miniature gearboxes" section. The side plates were fabricated by cutting 0.12-mm-thick pultruded carbon fiber strips (Van Dijk Pultrusion Products) with the laser cutter. The polymer film was laser cut from a 0.025-mm-thick polyimide film (Kapton HN, Dupont). The polymer films were sandwiched between two side plates using cyanoacrylate adhesive (Loctite 495). A 3D jig fabricated by two-photon polymerization aided the bonding between the flexure joints and the bottom plate (Fig. 3Bii). To achieve joints that require a full revolution, we adopted a pinhole design. This design was used to create the two-bar linkage and the connecting plate in the peristaltic robot (Fig. 3Ai), where the bars were fabricated with two-photon polymerization, and pins were cut from 0.1-mm-diameter acupuncture needles (S-J1015, Seirin Corporation).

To fabricate the latex spring for energy storage (Figs. 4Ai and 5, Ai and Bi), we followed three steps. First, a piece of latex cut from a latex glove (Latex comfort, Rotiprotect) was attached to the tape (Polyimide Tape 8897, 3M). Second, the taped latex sheet was laser cut into strips. Third, the latex strip was rolled into a circle using a 0.6-mm-diameter rod and glued end to end with the cyanoacrylate adhesive.

The elastic chamber for liquid storage (Fig. 5Ci) and part 1 (fig. S14Bi) of the pneumatic bending actuator were fabricated via casting (Dragon Skin 10, Smooth-On). Part 2 of the pneumatic bending actuator (fig. S14Bi) was fabricated by laser cutting a 50-μm-thick PDMS film, which was bonded to part 1 using uncured polymers (Dragon Skin 10, Smooth-On). The pneumatic expansion actuator was created by bonding thin polymer films together. The thin polymer films were fabricated by laser cutting a 100-μm-thick film (Dragon Skin 10, Smooth-On).

Magnetic actuation setups

The gearboxes were actuated via the rotating magnetic field generated by rotating permanent magnets, as shown in fig. S3. First, rotation of a single permanent magnet was used to generate such a magnetic field, which is the simplest and most flexible way and can be easily adapted to different application scenarios. It can also produce a strong magnetic field gradient to pull the gearbox toward the substrate, making it particularly suitable to enhance the stability of the gearbox during the actuation. The needle sampling and liquid sampling robots were actuated via a cube magnet (20 mm by 20 mm by 20 mm; MagnetMax) mounted on a DC motor (RE 40, Maxon).

Second, a cylindrical Halbach array was used to generate a more uniform rotating magnetic field in the actuation plane. It was mounted on a DC motor (2668W024CR, Faulhaber) with a gearhead (reduction of 3:1; 32GPT, Faulhaber). By controlling the drive voltage, we regulated the speed of the DC motor, enabling the control of the actuation frequency. The magnetic field strength was adjusted by changing the position of the magnetic disk with respect to the permanent magnets. A two-degree-of-freedom (two-DOF) translation stage (two-axis configurations of XR25C, Thorlabs) was used to adjust the actuation magnetic field strength by precisely adjusting the distance to the gearbox. The cylindrical Halbach array is useful for various experiments where uniform magnetic fields are desired, such as weight-lifting experiments and experiments on jumping and gripping robots.

Last, two antisymmetrically placed permanent magnets were used to drive the peristaltic robot. The magnetic field produced by this setup is weaker than those of the single permanent magnet and the Halbach array cylinder and is less uniform than the latter. However, a very high rotating speed can be achieved because of its small rotational inertia, which is suitable for applications where a high actuation frequency is desired.

Note that the magnetic field gradient still exists in the actuation plane (*xy*) of all of these actuation setups. Magnetic gradient forces in the actuation plane may direct the robot to undesired orientations. By increasing the distance between the robot and the permanent magnets, the undesired influence of the magnetic field gradient will be reduced.

Gearbox performance characterization

In the weight-lifting experiments, the output torque, τ_{lift}, is calculated by

$$\tau_{lift} = (m_{weight}g - F_b) \times (r_{shaft} + r_{thread}) \quad (1)$$

where g is the gravitational acceleration. r_{shaft} and r_{thread} are the radii of the output shaft cross section and the thread tethering the weight, which are 0.15 and 0.03 mm, respectively. F_b is the buoyant force acting on the weights. It was assumed to be zero when characterizations were conducted in air. The rotational speed of the output shaft is obtained by dividing the rotational speed of the magnetic field by the reduction ratio of the gearbox. The rotational speed of the output shaft is used to calculate the output power.

The overall transmission efficiency of the gearbox $\eta_{gearbox}$ in the weight-lifting experiment is defined as

$$\eta_{gearbox} = \frac{\tau_{lift}}{\tau_m n_{gearbox}} \quad (2)$$

where $n_{gearbox}$ is the reduction ratio of the gearbox. The magnetic torque τ_m acting on the input shaft can be expressed as

$$\tau_m = |V\mathbf{M} \times \mathbf{B}| \quad (3)$$

where V and $\mathbf{M}$ are volume and magnetization of the magnetic disk, respectively.

The experimental setup for weight-lifting experiments is illustrated in fig. S4. A high-speed camera was used to concurrently capture the rotational motions of the cylindrical Halbach array and the magnetic disk. The angle between the magnetization vectors at a certain time instant was measured from the high-speed images. The magnetization of the magnetic disk was measured using a VSM (EZ7, MicroSense). The average magnetic input torque was calculated by averaging the magnetic input torques measured from 10 time instants with equal time intervals within one rotation period of the magnetic disk. The magnetic input torque and the rotational speed of the magnetic field were used to calculate the input power.

Numerical simulations

To evaluate how different factors influence the gear meshing, we established a 3D dynamic implicit contact model of a gear pair using the finite element method (fig. S8Ai). The module and the teeth number were consistent with gear 2 and gear 3 of the gearbox (table S1).

The materials of the gears and the shafts were modeled as linear elastic materials. The Young's moduli of the epoxy gears, IP-S gears, and shafts were 49.6, 5.11, and 210 GPa, respectively. The Poisson's ratio for all parts was set to 0.3. The linear hexahedral element (C3D8R) was adopted for the mesh. The meshes around the gear teeth contact point and the gear teeth roots were refined (*60*). The total number of elements is 122,400, with 147,180 nodes. The contact between the driving gear and the driven gear was implemented using the surface-to-surface interactions available in ABAQUS/Standard. The penalty approach was adopted for modeling the tangential contact response, with the friction coefficient μ_1 applied to the tooth surfaces in meshing. The normal contact behavior was assigned a hard contact property (*61*). We further adopted two methods to account for the contact between the hole and shaft. In the first method, we applied the same contact model as that between two gears during the simulation. This method is time-consuming and can only be applied in benchmark cases. In the second method, we accounted for the contact between the hole and the shaft after the simulation. Specifically, the force acting on the hole due to gear meshing was obtained from the simulation results and used to calculate the resistance torque due to the friction between the hole and the shaft following the Coulomb friction law. Such resistance torque was then subtracted from the input torque obtained in simulation. We compared both methods in benchmark simulations, and the obtained transmission efficiencies were very close. The second method was applied to all simulations other than benchmark cases. In both methods, the friction coefficient between the hole and the shaft was set to be μ_2.

Figure S8A shows the boundary conditions of the geometry model for the second method, where two reference points located at the center of mass of the gear pair were kinematically coupled to the inner ring. A loading torque T_a was applied to the axial rotational DOF, whereas an angular velocity ω was added to the axial rotational DOF of the driving gear. In the first method, two shafts were included in the geometry model, where two other reference points located at the center of the end face of the shaft were coupled to the shaft surface through kinematic coupling. A concentrated force F (gravity of the weights in the benchmark experiments) was applied to the reference node of the driven gear. All DOFs of two reference nodes on the shafts were constrained (*62*), and the translational DOFs of gears in the *yz* plane were released.

Three analysis steps were created for both methods, of which the first two steps with shorter time periods were set to improve contact convergence (*60*). Specifically, from 0 to 0.008 s (step 1), ω was gradually increased from 0 to 2π rad/s to establish a smooth contact. From 0.05 to 0.5 s (step 2), T_a was gradually increased from 0 to the target value. In step 3, loading torque T_a (and the concentrated force F in the first method) and angular velocity ω were applied instantaneously. The nonlinear effects of the large deformation and displacements of the gears were considered, and the full-Newton algorithm was used for the implicit time integration in the dynamic analysis.

In the first method, the transmission efficiency η is calculated by the following equation:

$$\eta = \frac{T_a}{n\overline{T_r}} \quad (4)$$

where n is the gear ratio and $\overline{T_r}$ is the mean reaction torque of the driving gear during a meshing cycle (from t_0 to t_1) (fig. S8B)

$$\overline{T_r} = \int_{t_0}^{t_1} T_r(t)\,dt \Big/ (t_1 - t_0) \quad (5)$$

In the second method, η is calculated as follows:

$$\eta = \frac{T_a - \overline{T_f}}{n(\overline{T_r} + \overline{T_f})} \quad (6)$$

where $\overline{T_f}$ is the mean torque produced by the friction between the shaft and the gear during a meshing cycle

$$\overline{T_f} = \mu_2 R_p \int_{t_0}^{t_1} F_n(t)\,dt \Big/ (t_1 - t_0) \quad (7)$$

where F_n is the normal force applied to gear and R_p is the radius of the shaft (fig. S8Ai).

The RMSD of the time-history meshing force F is used to quantify the oscillation of the gear meshing force:

$$\mathrm{RMSD} = \sqrt{\frac{1}{N}\sum_{i=1}^{N}(F_i - \overline{F})^2} \quad (8)$$

where F_i is the output meshing force at the time instant i, $\overline{F}$ is the mean value of the time-history resultant mesh force F, and N is the total number of the discretized time instants in a meshing cycle.

To estimate the fluid torque resistance acting on the magnetic disk, we conducted a frozen rotor analysis in COMSOL Multiphysics (COMSOL 6.0, COMSOL Inc.). The fluid torque resistance was calculated by integrating the hydrodynamic force over the outer surface of the magnetic disk. The mesh and the boundary conditions used in the simulation are illustrated in fig. S6A. The rotational speed of the magnetic disk was set from 1 to 50 revolutions per second with an interval of 10. The viscosities of the water and the glycerol solution [glycerol:water = 6:1 (v/v)] were set to be 8.9274×10^{-4} and 0.12355 Pa·s, respectively (*63*). The results are reported in fig. S6B. The magnetic fields around the magnetic setups (fig. S3) were investigated by conducting magnetostatic field simulation in COMSOL Multiphysics.

Friction coefficient measurements

Friction coefficient measurements were performed in a custom setup, as shown in fig. S7A. The test samples consisted of a 1-mm-diameter hemisphere and a thin sheet substrate. Polymer samples of different materials were fabricated via two-photon polymerization or casting. Stainless steel sheet samples were laser cut from a 50-μm-thick stainless steel. The normal and friction forces were measured with load cells (GSO-25, Transducer Techniques, LSB200, FUTEK Advanced Sensor Technology). The hemisphere of the sample was mounted on the load cell. Its z-direction movement was controlled by a motorized linear stage (LPS-65 2″, Physik Instrumente GmbH & Co. KG) with a 5-nm position resolution to apply a normal force to the substrate. The substrate of the sample was mounted on another x-direction linear stage. A custom LabVIEW (National Instruments Corporation) code allowed displacement and velocity control in both x and z directions. Three steps were followed for the measurements: First, the hemisphere was controlled to approach the substrate at a speed of 20 μm/s until a 3-mN preload was reached. Second, the substrate was controlled to move at 20 μm/s until a 0.5-mm displacement was reached. Third, the hemisphere was lifted. The measurement data used for calculating the friction coefficients were obtained from the second step.

Statistical tests

Experimental values measured N times were reported in the figures as means ± SD. One-way ANOVA was applied to determine whether there were any statistically significant differences between the means of the transmission efficiencies measured at different actuation frequencies. For single measurement experiments ($N = 1$), only the measurement values were reported.

SUPPLEMENTARY MATERIALS

www.science.org/doi/10.1126/scirobotics.abo4401
Supplementary Discussion
Table S1
Figs. S1 to S14
Movies S1 to S9
References (*64*–*94*)

REFERENCES AND NOTES

1. M. P. Kummer, J. J. Abbott, B. E. Kratochvil, R. Borer, A. Sengul, B. J. Nelson, OctoMag: An electromagnetic system for 5-DOF wireless micromanipulation. *IEEE Trans. Robot.* **26**, 1006–1017 (2010).
2. E. Diller, J. Giltinan, G. Z. Lum, Z. Ye, M. Sitti, Six-degree-of-freedom magnetic actuation for wireless microrobotics. *Int. J. Robot. Res.* **35**, 114–128 (2016).
3. G. Z. Lum, Z. Ye, X. Dong, H. Marvi, O. Erin, W. Hu, M. Sitti, Shape-programmable magnetic soft matter. *Proc. Natl. Acad. Sci. U.S.A.* **113**, E6007–E6015 (2016).
4. W. Hu, G. Z. Lum, M. Mastrangeli, M. Sitti, Small-scale soft-bodied robot with multimodal locomotion. *Nature* **554**, 81–85 (2018).
5. Z. Ren, R. Zhang, R. H. Soon, Z. Liu, W. Hu, P. R. Onck, M. Sitti, Soft-bodied adaptive multimodal locomotion strategies in fluid-filled confined spaces. *Sci. Adv.* **7**, eabh2022 (2021).
6. X. Bao, W. Li, M. Lu, Z. R. Zhou, Experiment study on puncture force between MIS suture needle and soft tissue. *Biosurf. Biotribol.* **2**, 49–58 (2016).
7. T. W. Duerig, D. E. Tolomeo, M. Wholey, An overview of superelastic stent design. *Minim. Invasive Ther. Allied Technol.* **9**, 235–246 (2000).
8. S. Baik, D. W. Kim, Y. Park, T. J. Lee, S. Ho Bhang, C. Pang, A wet-tolerant adhesive patch inspired by protuberances in suction cups of octopi. *Nature* **546**, 396–400 (2017).
9. M. Sitti, D. S. Wiersma, Pros and cons: Magnetic versus optical microrobots. *Adv. Mater.* **32**, 1906766 (2020).
10. M. Sitti, *Mobile Microrobotics* (MIT Press, 2017).
11. S. Tumanski, Modern magnetic materials—The review. *Prz. Elektrotechniczny* **86**, 1–15 (2010).
12. H. J. Lu, M. Zhang, Y. Yang, Q. Huang, T. Fukuda, Z. Wang, Y. Shen, A bioinspired multilegged soft millirobot that functions in both dry and wet conditions. *Nat. Commun.* **9**, 3944 (2018).
13. M. Sitti, H. Ceylan, W. Hu, J. Giltinan, M. Turan, S. Yim, E. Diller, Biomedical applications of untethered mobile milli/microrobots. *Proc. IEEE* **103**, 205–224 (2015).
14. D. Son, M. C. Ugurlu, M. Sitti, Permanent magnet array–driven navigation of wireless millirobots inside soft tissues. *Sci. Adv.* **7**, eabi8932 (2021).
15. J. Rahmer, C. Stehning, B. Gleich, Remote magnetic actuation using a clinical scale system. *PLOS ONE* **13**, e0193546 (2018).
16. A. Azizi, C. C. Tremblay, K. Gagné, S. Martel, Using the fringe field of a clinical MRI scanner enables robotic navigation of tethered instruments in deeper vascular regions. *Sci. Robot.* **4**, eaax7342 (2019).
17. M. E. Tiryaki, M. Sitti, Magnetic resonance imaging-based tracking and navigation of submillimeter-scale wireless magnetic robots. *Adv. Intell. Syst.* **4**, 2100178 (2021).
18. S. Hahn, K. Kim, K. Kim, X. Hu, T. Painter, I. Dixon, S. Kim, K. R. Bhattarai, S. Noguchi, J. Jaroszynski, D. C. Larbalestier, 45.5-tesla direct-current magnetic field generated with a high-temperature superconducting magnet. *Nature* **570**, 496–499 (2019).
19. Y. Alapan, U. Bozuyuk, P. Erkoc, A. C. Karacakol, M. Sitti, Multifunctional surface microrollers for targeted cargo delivery in physiological blood flow. *Sci. Robot.* **5**, eaba5726 (2020).
20. T. Mayer, J. Elam, S. George, P. Kotula, R. Goeke, Atomic-layer deposition of wear-resistant coatings for microelectromechanical devices. *Appl. Phys. Lett.* **82**, 2883–2885 (2003).
21. T. Grzebyk, MEMS vacuum pumps. *J. Microelectromech. Syst.* **26**, 705–717 (2017).
22. S. Zhang, M. Elsayed, R. Peng, Y. Chen, Y. Zhang, J. Peng, W. Li, M. D. Chamberlain, A. Nikitina, S. Yu, X. Liu, S. L. Neale, A. R. Wheeler, Reconfigurable multi-component micromachines driven by optoelectronic tweezers. *Nat. Commun.* **12**, 5349 (2021).
23. G. Vizsnyiczai, G. Frangipane, C. Maggi, F. Saglimbeni, S. Bianchi, R. D. Leonardo, Light controlled 3D micromotors powered by bacteria. *Nat. Commun.* **8**, 15974 (2017).
24. Y. Kadota, K. Inoue, K. Uzuka, H. Suenaga, T. Morita, Noncontact operation of a miniature cycloid motor by magnetic force. *IEEE/ASME Trans. Mechatron.* **18**, 1563–1571 (2012).
25. P. Vartholomeos, C. Bergeles, L. Qin, P. E. Dupont, An MRI-powered and controlled actuator technology for tetherless robotic interventions. *Int. J. Robot. Res.* **32**, 1536–1552 (2013).
26. W. T. Townsend, J. K. Salisbury, Mechanical design for whole-arm manipulation, in *Robots and Biological Systems: Towards a New Bionics?* (Springer, 1993), pp. 153–164.
27. D. Shah, A. Parmiggiani, Y.-J. Kim, Constant length tendon routing mechanism through axial joint, in *Proceedings of the 2020 IEEE/ASME International Conference on Advanced Intelligent Mechatronics (AIM)* (IEEE, 2020), pp. 753–758.
28. K. Salisbury, W. Townsend, B. Ebrman, D. DiPietro, Preliminary design of a whole-arm manipulation system (WAMS), in *Proceedings of the 1988 IEEE International Conference on Robotics and Automation* (IEEE, 1988), pp. 254–260.
29. R. Y. Hutama, M. M. Khalil, T. Mashimo, A millimeter-scale rolling microrobot driven by a micro-geared ultrasonic motor. *IEEE Robot. Autom. Lett.* **6**, 8158–8164 (2021).
30. T. Mashimo, T. Urakubo, Y. Shimizu, Micro geared ultrasonic motor. *IEEE/ASME Trans. Mechatron.* **23**, 781–787 (2018).
31. E. Saerens, S. Crispel, P. L. García, T. Verstraten, V. Ducastel, B. Vanderborght, D. Lefeber, Scaling laws for robotic transmissions. *Mech. Mach. Theory* **140**, 601–621 (2019).

32. N. Hosoda, S. N. Gorb, Underwater locomotion in a terrestrial beetle: Combination of surface de-wetting and capillary forces. *Proc. Biol. Sci.* **279**, 4236–4242 (2012).
33. D. Miler, A. Lončar, D. Žeželj, Z. Domitran, Influence of profile shift on the spur gear pair optimization. *Mech. Mach. Theory* **117**, 189–197 (2017).
34. N. Saga, T. Nakamura, Development of a peristaltic crawling robot using magnetic fluid on the basis of the locomotion mechanism of the earthworm. *Smart Mater. Struct.* **13**, 566–569 (2004).
35. M. Kamata, S. Yamazaki, Y. Tanise, Y. Yamada, T. Nakamura, Morphological change in peristaltic crawling motion of a narrow pipe inspection robot inspired by earthworm's locomotion. *Adv. Robot.* **32**, 386–397 (2018).
36. T. Nakamura, Y. Hidaka, M. Yokojima, K. Adachi, Development of peristaltic crawling robot with artificial rubber muscles attached to large intestine endoscope. *Adv. Robot.* **26**, 1161–1182 (2012).
37. A. Kandhari, Y. F. Wang, H. J. Chiel, R. D. Quinn, K. A. Daltorio, An analysis of peristaltic locomotion for maximizing velocity or minimizing cost of transport of earthworm-like robots. *Soft Robot.* **8**, 485–505 (2021).
38. H. Banerjee, N. Pusalkar, H. L. Ren, Single-motor controlled tendon-driven peristaltic soft origami robot. *J. Mech. Robot.* **10**, 064501 (2018).
39. P. Bhovad, J. Kaufmann, S. Y. Li, Peristaltic locomotion without digital controllers: Exploiting multi-stability in origami to coordinate robotic motion. *Extreme Mech. Lett.* **32**, 100552 (2019).
40. B. L. Deng, L. Y. Chen, D. L. Wei, V. Tournat, K. Bertoldi, Pulse-driven robot: Motion via solitary waves. *Sci. Adv.* **6**, eaaz1166 (2020).
41. M. P. Nemitz, P. Mihaylov, T. W. Barraclough, D. Ross, A. A. Stokes, Using voice coils to actuate modular soft robots: Wormbot, an example. *Soft Robot.* **3**, 198–204 (2016).
42. S. Seok, C. D. Onal, K. J. Cho, R. J. Wood, D. Rus, S. Kim, Meshworm: A peristaltic soft robot with antagonistic nickel titanium coil actuators. *IEEE/ASME Trans. Mechatron.* **18**, 1485–1497 (2013).
43. Z. F. Sun, Y. Yamauchi, F. Araoka, Y. S. Kim, J. Bergueiro, Y. Ishida, Y. Ebina, T. Sasaki, T. Hikima, T. Aida, An anisotropic hydrogel actuator enabling earthworm-like directed peristaltic crawling. *Angew. Chem. Int. Ed.* **57**, 15772–15776 (2018).
44. Q. L. Zhu, C. Du, Y. Dai, M. Daab, M. Matejdes, J. Breu, W. Hong, Q. Zheng, Z. L. Wu, Light-steered locomotion of muscle-like hydrogel by self-coordinated shape change and friction modulation. *Nat. Commun.* **11**, 5166 (2020).
45. S. Palagi, A. G. Mark, S. Y. Reigh, K. Melde, T. Qiu, H. Zeng, C. Parmeggiani, D. Martella, A. Sanchez-Castillo, N. Kapernaum, F. Giesselmann, D. S. Wiersma, E. Lauga, P. Fischer, Structured light enables biomimetic swimming and versatile locomotion of photoresponsive soft microrobots. *Nat. Mater.* **15**, 647–653 (2016).
46. S. J. Kim, D. Y. Lee, G. P. Jung, K. J. Cho, An origami-inspired, self-locking robotic arm that can be folded flat. *Sci. Robot.* **3**, eaar2915 (2018).
47. C. Tang, B. Du, S. Jiang, Q. Shao, X. Dong, X.-J. Liu, H. Zhao, A pipeline inspection robot for navigating tubular environments in the sub-centimeter scale. *Sci. Robot.* **7**, eabm8597 (2022).
48. A. Biewener, S. Patek, *Animal Locomotion* (Oxford Univ. Press, 2018).
49. E. Steinhardt, N. S. P. Hyun, J. S. Koh, G. Freeburn, M. H. Rosen, F. Z. Temel, S. N. Patek, R. J. Wood, A physical model of mantis shrimp for exploring the dynamics of ultrafast systems. *Proc. Natl. Acad. Sci. U.S.A.* **118**, e2026833118 (2021).
50. S. M. Baek, S. Yim, S. H. Chae, D. Y. Lee, K. J. Cho, Ladybird beetle-inspired compliant origami. *Sci. Robot.* **5**, eaaz6262 (2020).
51. M. A. Woodward, M. Sitti, Multimo-bat: A biologically inspired integrated jumping–gliding robot. *Int. J. Robot. Res.* **33**, 1511–1529 (2014).
52. M. Li, X. Wang, B. Dong, M. Sitti, In-air fast response and high speed jumping and rolling of a light-driven hydrogel actuator. *Nat. Commun.* **11**, 3988 (2020).
53. D. Son, H. Gilbert, M. Sitti, Magnetically actuated soft capsule endoscope for fine-needle biopsy. *Soft Robot.* **7**, 10–21 (2020).
54. Y. Yoshioka, N. Kosaka, Y. Konishi, H. Ohta, H. Okamoto, H. Sonoda, R. Nonaka, H. Yamamoto, H. Ishii, M. Mori, K. Furuta, T. Nakajima, H. Hayashi, H. Sugisaki, H. Higashimoto, T. Kato, F. Takeshita, T. Ochiy, Ultra-sensitive liquid biopsy of circulating extracellular vesicles using ExoScreen. *Nat. Commun.* **5**, 3591 (2014).
55. M. Ignatiadis, G. W. Sledge, S. S. Jeffrey, Liquid biopsy enters the clinic—Implementation issues and future challenges. *Nat. Rev. Clin. Oncol.* **18**, 297–312 (2021).
56. V. Iacovacci, I. Tamadon, E. F. Kauffmann, S. Pane, V. Simoni, L. Marziale, M. Aragona, L. Cobuccio, M. Chiarugi, P. Dario, S. D. Prato, L. Ricotti, F. Vistoli, A. Menciassi, A fully implantable device for intraperitoneal drug delivery refilled by ingestible capsules. *Sci. Robot.* **6**, eabh3328 (2021).
57. L. Hines, K. Petersen, G. Z. Lum, M. Sitti, Soft actuators for small-scale robotics. *Adv. Mater.* **29**, 1603483 (2017).
58. N. El-Atab, R. B. Mishra, F. Al-Modaf, L. Joharji, A. A. Alsharif, H. Alamoudi, M. Diaz, N. Qaiser, M. M. Hussain, Soft actuators for soft robotic applications: A review. *Adv. Intell. Syst.* **2**, 2000128 (2020).
59. E. W. Hawkes, C. Xiao, R. A. Peloquin, C. Keeley, M. R. Begley, M. T. Pope, G. Niemeyer, Engineered jumpers overcome biological limits via work multiplication. *Nature* **604**, 657–661 (2022).
60. G. J. Wang, L. Chen, L. Yu, S. D. Zou, Research on the dynamic transmission error of a spur gear pair with eccentricities by finite element method. *Mech. Mach. Theory* **109**, 1–13 (2017).
61. C. Zhou, C. Chen, L. Gui, Z. Fan, A nonlinear multi-point meshing model of spur gears for determining the face load factor. *Mech. Mach. Theory* **126**, 210–224 (2018).
62. X. Hu, B. Hu, F. Zhang, B. Fu, H. Li, Y. Zhou, Influences of spline assembly methods on nonlinear characteristics of spline–gear system. *Mech. Mach. Theory* **127**, 33–51 (2018).
63. N.-S. Cheng, Formula for the viscosity of a glycerol–water mixture. *Ind. Eng. Chem. Res.* **47**, 3285–3288 (2008).
64. T. Mashimo, Micro ultrasonic motor using a cube with a side length of 0.5 mm. *IEEE/ASME Trans. Mechatron.* **21**, 1189–1192 (2016).
65. G. Rogers, Three degree-of-freedom piezoelectric ultrasonic micro-motor with a major diameter of 350 μm. *J. Micromech. Microeng.* **20**, 125002 (2010).
66. L. Yan, D. L. Liu, H. Lan, Z. X. Jiao, Compact traveling wave micromotor based on shear electromechanical coupling. *IEEE/ASME Trans. Mechatron.* **21**, 1572–1580 (2016).
67. L. Yan, H. Lan, Z. X. Jiao, C. Y. Chen, I. M. Chen, Compact piezoelectric micromotor with a single bulk lead zirconate titanate stator. *Appl. Phys. Lett.* **102**, 134106 (2013).
68. T. Mashimo, Performance evaluation of a micro ultrasonic motor using a one-cubic-millimeter stator. *IEEE Trans. Ultrason. Ferroelectr. Freq. Control* **62**, 1819–1826 (2015).
69. T. Mashimo, Y. Oba, Performance improvement of micro-ultrasonic motors using the thickness shear mode piezoelectric elements. *Sens. Actuat A Phys.* **335**, 113347 (2022).
70. B. Watson, J. Friend, L. Yeo, Piezoelectric ultrasonic resonant motor with stator diameter less than 250 μm: The Proteusmotor. *J. Micromech. Microeng.* **19**, 022001 (2009).
71. R. Q. Rudy, G. L. Smith, D. L. DeVoe, R. G. Polcawich, Millimeter-scale traveling wave rotary ultrasonic motors. *J. Microelectromech. Syst.* **24**, 108–114 (2015).
72. T. Kanda, A. Makino, T. Ono, K. Suzumori, T. Morita, M. K. Kurosawa, A micro ultrasonic motor using a micro-machined cylindrical bulk PZT transducer. *Sens. Actuat. A Phys.* **127**, 131–138 (2006).
73. H. Zhang, S. Dong, S. Zhang, T. Wang, Z. Zhang, L. Fan, Ultrasonic micro-motor using miniature piezoelectric tube with diameter of 1.0 mm. *Ultrasonics* **44**, E603–E606 (2006).
74. Y. T. Ma, M. Choi, K. Uchino, Single-phase driven ultrasonic motor using two orthogonal bending modes of sandwiching piezo-ceramic plates. *Rev. Sci. Instrum.* **87**, 115004 (2016).
75. A. Gour, M. Menard, F. Nabki, High torque electrostatic micromotor fabricated using polymumps for optical scanning applications, in *Proceedings of the 2021 34th IEEE International Conference on Micro Electro Mechanical Systems (MEMS)* (IEEE, 2021), pp. 716–719.
76. S. Lee, D. Kim, M. D. Bryant, F. F. Ling, A micro corona motor. *Sens. Actuat. A Phys.* **118**, 226–232 (2005).
77. W. Liu, W. P. Zhang, W. Y. Chen, Simulation analysis and experimental study of the diamagnetically levitated electrostatic micromotor. *J. Magn. Magn. Mater.* **492**, 165634 (2019).
78. A. Geisberger, D. Kadylak, M. Ellis, A silicon electrothermal rotational micro motor measuring one cubic millimeter. *J. Micromech. Microeng.* **16**, 1943–1950 (2006).
79. J. Peng, L. C. Ma, H. Tang, S. P. Chen, A micro self-spin electromagnetic actuator for intravascular ultrasound (IVUS) imaging application, in *Proceedings of the IEEE International Ultrasonics Symposium (IUS)* (IEEE, 2017), pp. 1–4.
80. J. Peng, Z. Qin, S. Chen, Design and fabrication of an electromagnetic micro-motor for intravascular ultrasound (IVUS) imaging, in *Proceedings of the 2016 IEEE International Ultrasonics Symposium (IUS)* (IEEE, 2016), pp. 1–4.
81. A. Inoue, B. L. Shen, A. Takeuchi, Developments and applications of bulk glassy alloys in late transition metal base system. *Mater. Trans.* **47**, 1275–1285 (2006).
82. K. Hori, T. Miyagawa, K. Ito, Development of ultra-small sized servo actuator with brushless DC motor, planetary gear drive and optical rotary encoder. *Int. J. Jpn. Soc. Precis. Eng.* **63**, 1073–1076 (1997).
83. D. Han, K. Nagai, T. Shinshi, Micro electromagnetic flat motor using an 80-poles and 0.3-mm-thick ring magnet for high torque, in *Proceedings of the IEEE 33rd International Conference on Micro Electro Mechanical Systems (MEMS)* (IEEE, 2020), pp. 509–512.
84. J. S. Koh, S. P. Jung, R. J. Wood, K. J. Cho, A jumping robotic insect based on a torque reversal catapult mechanism, in *IEEE/RSJ International Conference on Intelligent Robots and Systems* (IEEE, 2013), pp. 3796–3801.
85. M. Noh, S. W. Kim, S. An, J. S. Koh, K. J. Cho, Flea-inspired catapult mechanism for miniature jumping robots. *IEEE Trans. Robot.* **28**, 1007–1018 (2012).
86. M. Kovac, M. Fuchs, A. Guignard, J. C. Zufferey, D. Floreano, A miniature 7g jumping robot, in *Proceedings of the IEEE International Conference on Robotics and Automation* (IEEE, 2008), pp. 373–378.
87. Z. Zhakypov, K. Mori, K. Hosoda, J. Paik, Designing minimal and scalable insect-inspired multi-locomotion millirobots. *Nature* **571**, 381–386 (2019).

88. J. M. Morrey, B. Lambrecht, A. D. Horchler, R. E. Ritzmann, R. D. Quinn, Highly mobile and robust small quadruped robots, in *Proceedings of the 2003 IEEE/RSJ International Conference on Intelligent Robots and Systems* (IEEE, 2003), vol 1, pp. 82–87.
89. Y. Sugiyama, S. Hirai, Crawling and jumping by a deformable robot. *Int. J. Robot. Res.* **25**, 603–620 (2006).
90. J. G. Zhao, W. H. Yan, N. Xi, M. W. Mutka, L. Xiao, A miniature 25 grams running and jumping robot, in *Proceedings of the IEEE International Conference on Robotics and Automation* (IEEE, 2014), pp. 5115–5120.
91. Z. W. Yu, Y. F. Zeng, C. Guo, Mechanical design and performance analysis of a weevil-inspired jumping mechanism. *Machines* **10**, 161 (2022).
92. G. P. Jung, C. S. Casarez, S. P. Jung, R. S. Fearing, K. J. Cho, An integrated jumping-crawling robot using height-adjustable jumping module, in *IEEE International Conference on Robotics and Automation* (IEEE, 2016), pp. 4680–4685.
93. M. A. Woodward, M. Sitti, Universal custom complex magnetic spring design methodology. *IEEE Trans. Magn.* **54**, 1–13 (2018).
94. W. Wu, X. Chen, Y. Shan, Analysis and experiment of a vibration isolator using a novel magnetic spring with negative stiffness. *J. Sound Vibr.* **333**, 2958–2970 (2014).

Acknowledgments: We thank N. Krishna-Subbaiah and A. Shiva for assistance in experiments. **Funding:** This work is funded by the Max Planck Society, European Research Council (ERC) Advanced Grant SoMMoR project with grant no. 834531, and German Research Foundation (DFG) Soft Material Robotic Systems (SPP 2100) Program with grant no. 2197/3-1. C.H. thanks the China Scholarship Council (grant no. 202006120160) for financial support. **Author contributions:** C.H., Z.R., W.H., and M.S. proposed and designed the research. C.H. and Z.R. performed the experiments and analyzed the data with the help of M.L., Y.W., and D.T. Simulations were performed by C.H. and C.W. The manuscript was written by C.H., Z.R., W.H., and M.S. **Competing interests:** The authors declare that they have no competing financial interests. **Data and materials availability:** All data needed to evaluate the conclusions in the paper are presented in the paper and the Supplementary Materials and are available online in https://doi.org/10.5061/dryad.2fqz612s9.

Submitted 3 February 2022
Accepted 3 August 2022
Published 31 August 2022
10.1126/scirobotics.abo4401

Science Robotics

Magnetically actuated gearbox for the wireless control of millimeter-scale robots

Chong Hong, Ziyu Ren, Che Wang, Mingtong Li, Yingdan Wu, Dewei Tang, Wenqi Hu, and Metin Sitti

Sci. Robot. **7** (69), eabo4401. DOI: 10.1126/scirobotics.abo4401

Science Robotics (ISSN 2470-9476) is published by the American Association for the Advancement of Science. 1200 New York Avenue NW, Washington, DC 20005. The title *Science Robotics* is a registered trademark of AAAS.